JGR Solid Earth

RESEARCH ARTICLE
10.1029/2025JB031599

Imaging of Magma Intrusion Below La Palma During a Strong Effusive Eruption in 2021 Inferred From Repeated Seismic Tomography

Ivan Koulakov[1,2], **Luca D'Auria**[3,4], **and Jesús M. Ibáñez**[5,6]

[1]Center for Petroleum Science and Engineering, Skolkovo Institute of Science and Technology (Skoltech), Moscow, Russia, [2]Trofimuk Institute of Petroleum Geology and Geophysics (IPGG) SB RAS, Novosibirsk, Russia, [3]Instituto Volcanológico de Canarias (INVOLCAN), San Cristóbal de la Laguna, Spain, [4]Instituto Tecnológico y de Energías Renovables (ITER), Granadilla de Abona, Spain, [5]Faculty of Sciences, Department of Theoretical Physics and the Cosmos, University of Granada, Granada, Spain, [6]Andalusian Institute of Geophysics, Universidad de Granada, Granada, Spain

Abstract The 2021 eruption of Cumbre Vieja on La Palma, Canary Islands, provided a unique opportunity to investigate the dynamics of magma migration and storage during a large effusive eruption. In this study, we employ repeated seismic tomography to image temporal changes in the subsurface structure beneath La Palma, using body-wave travel times from local earthquakes recorded before and during the eruption. By carefully selecting paired data sets with identical numbers of events and similar ray path distributions, we minimize biases introduced by variations in seismicity patterns and ensure robust detection of velocity changes. Our results reveal a complex magma plumbing system characterized by a deep magma storage zone below 8 km depth and a shallow, fluid-saturated region extending to ~3 km depth. During the eruption, a high Vp/Vs anomaly, interpreted as a magma conduit, formed and ascended through a rigid barrier at 5–8 km depth, facilitating the transport of significant volumes of magma to the surface. The conduit evolved from a diapir-like structure with a stable head at 6–7 km depth in the early stages of the eruption to an ascending plume reaching 3 km depth in later stages. This study highlights the utility of repeated seismic tomography in unraveling the dynamic processes driving effusive eruptions and provides new insights into the evolution of magma systems during volcanic unrest.

Plain Language Summary The Cumbre Vieja effusive eruption occurred in September–November 2021 on La Palma was one of the most significant volcanic events in the Canary Islands' recent history. To study how the magma system evolves underground, we used a technique called repeated seismic tomography. This method analyzes earthquake waves recorded at different times, ensuring the data had similar coverage to minimize biases. By considering data from before and during the eruption, we tracked changes in the volcano's subsurface structure over time. Our results reveal that during the eruption, a magma pathway formed and rose through a rigid layer of rock between 5 and 8 km deep, enabling large volumes of magma to reach the surface. This pathway evolved over time, beginning as a stable, blob-like structure at 6–7 km deep and later rising closer to the surface as the eruption continued. We also identified two key features that remained unchanged during the eruption: a deep magma storage zone at about 8 km below the surface and a shallower, fluid-rich region extending down to about 3 km. This study highlights how repeated seismic imaging can provide new insights into the evolution of magma systems during large eruptions.

Key Points:

- Repeated seismic tomography uses earthquake body waves to image subsurface changes, using paired data sets with similar ray paths
- The repeated tomography reveals a magma conduit formed during the eruption, ascending through a rigid layer at 5–8 km depth
- We identified a deep magma storage below 8 km and a shallow fluid-rich zone above 3 km that remained nearly unchanged during the eruption

Supporting Information:

Supporting Information may be found in the online version of this article.

Correspondence to:

I. Koulakov,
ivan.science@gmail.com

Citation:

Koulakov, I., D'Auria, L., & Ibáñez, J. M. (2026). Imaging of magma intrusion below La Palma during a strong effusive eruption in 2021 inferred from repeated seismic tomography. *Journal of Geophysical Research: Solid Earth*, *131*, e2025JB031599. https://doi.org/10.1029/2025JB031599

Received 22 MAR 2025
Accepted 28 NOV 2025
Corrected 16 JAN 2026

This article was corrected on 16 JAN 2026. See the end of the full text for details.

Author Contributions:

Conceptualization: Jesús M. Ibáñez
Data curation: Luca D'Auria
Funding acquisition: Jesús M. Ibáñez
Project administration: Luca D'Auria, Jesús M. Ibáñez
Resources: Luca D'Auria
Software: Ivan Koulakov
Validation: Ivan Koulakov
Visualization: Ivan Koulakov
Writing – original draft: Ivan Koulakov
Writing – review & editing: Luca D'Auria, Jesús M. Ibáñez

1. Introduction

Volcanic eruptions are among the few natural phenomena capable of significantly altering the physical state of large underground volumes on a whole-crustal scale. Rapid intrusions of magma, fluid dynamics, and degassing can cause substantial changes in rock properties within timescales ranging from months to mere hours (e.g., Sparks et al., 2019). Detecting these changes through geophysical methods provides valuable insights into the underground processes driving volcanic eruptions.

In recent decades, numerous studies have investigated temporal changes beneath active volcanoes using seismic tomography. Two primary approaches have been employed: body-wave tomography, which utilizes seismic waves from local earthquakes, and ambient noise tomography, which relies on surface waves from ambient noise correlation.

The latter has been successfully applied to several volcanoes, including Piton de la Fournaise (Duputel et al., 2009; Sens-Schonfelder et al., 2014), Etna (Cannata et al., 2018), Kilauea (Donaldson et al., 2017; Olivier et al., 2019), Bezymianny (Berezhnev et al., 2023) and La Palma (Cabrera-Pérez et al., 2023). Ambient noise tomography offers distinct advantages over local earthquake tomography. Since it utilizes pairs of fixed stations as virtual sources and receivers, the ray configuration remains unchanged throughout the experiment, allowing direct identification of any temporal variations in the cross-correlation functions. However, this method is also subject to limitations. Changes in ambient noise distribution can affect cross-correlation results, potentially leading to misinterpretations. Additionally, surface wave tomography has limited lateral resolution, which decreases with depth. In many volcanic regions, magma reservoirs are located at depths of 3–5 km, where surface waves with periods of 3–7 s (wavelengths of 10–20 km) have insufficient sensitivity. Consequently, most temporal variations detected using this technique are confined to shallow layers, which are heavily influenced by seasonal effects (Sens-Schönfelder & Wegler, 2006). As a result, eruption-related changes in deeper structures are often weak and difficult to distinguish from other influences (Berezhnev et al., 2023; Sens-Schonfelder et al., 2014).

An alternative approach involves monitoring temporal changes in seismic velocity using body waves from local earthquakes. Several studies have employed this method to investigate subsurface variations beneath active volcanoes. For example, Patanè et al. (2006) conducted repeated tomography of Mount Etna and reported significant velocity changes in the volcano's edifice associated with the 2002–2003 flank eruption. Koulakov et al. (2013) analyzed the Klyuchevskoy volcano group in Kamchatka over 10 yearly intervals and found that Vp/Vs ratio variations in the middle and upper crust corresponded to eruption cycles at Klyuchevskoy and Bezymianny volcanoes. Similarly, Kasatkina et al. (2014) studied Mount Redoubt in Alaska, revealing that an S-wave velocity anomaly inside the edifice changed from strongly positive to negative, indicating fracturing and fluid saturation during the 2009 eruption.

Despite these findings, many studies using repeated tomography have not accounted for the potential biases introduced by uneven data distribution across different time periods. Variations in seismicity patterns, particularly during eruptions, can lead to differences in data coverage that may overshadow actual velocity changes related to geological processes. For example, an ongoing eruption can trigger increased seismicity along magma conduits. If repeated inversions are performed using data sets with and without eruption-related events, the resulting velocity contrasts may be misinterpreted as evidence of magma and fluid migration.

To mitigate this issue, Koulakov et al. (2016) developed an algorithm for selecting nearly identical data subsets for repeated tomography. This method was initially tested in the region of the Tohoku-Oki earthquake in Japan, where it revealed relatively minor velocity changes (less than 1%) in the upper crust, attributed to rock displacement, fracturing, and fluid saturation. A similar approach, adapted for regions with sparser data coverage, has been applied to several active volcanoes. For instance, Vargas et al. (2017) used repeated tomography at Nevado del Ruiz in Colombia and identified velocity changes within the magma reservoir associated with prolonged degassing activity. At Mount Spurr in Alaska, Koulakov et al. (2018) detected a rising high Vp/Vs anomaly, interpreted as fluid escape from the magma reservoir, which led to volcanic unrest in 2004–2006. Likewise, Koulakov and Vargas (2018) studied Galeras Volcano in Colombia, revealing a conduit that became evident during increased eruption activity from 2005 to 2010.

In this study, we apply a similar approach—repeated tomography with carefully selected, nearly identical data subsets—to examine the underground dynamics beneath La Palma Island during its major effusive eruption from September to November 2021. Previous work by D'Auria et al. (2022) constructed a detailed tomography model using local earthquake data collected throughout the eruption. However, if significant changes in rock properties occurred during the eruption, a single inversion using data from before and during the eruption could introduce artifacts due to unaccounted temporal variations.

Several factors make the La Palma eruption a particularly compelling case for repeated tomography. First, the eruption was monitored with a dense seismic network, consisting of 23 permanent stations strategically positioned around the active vents (Figure 1). In contrast, previous repeated tomography studies of other volcanoes often relied on less favorable network configurations, limiting tomography resolution. Second, the La Palma eruption evolved rapidly. Seismicity patterns indicate that magma migration occurred within just 1 week prior to the eruption, and the most intense lava effusion began immediately after the vent opened on 19 September 2021. This distinct separation between pre- and syn-eruption stages contrasts with other volcanic events, which

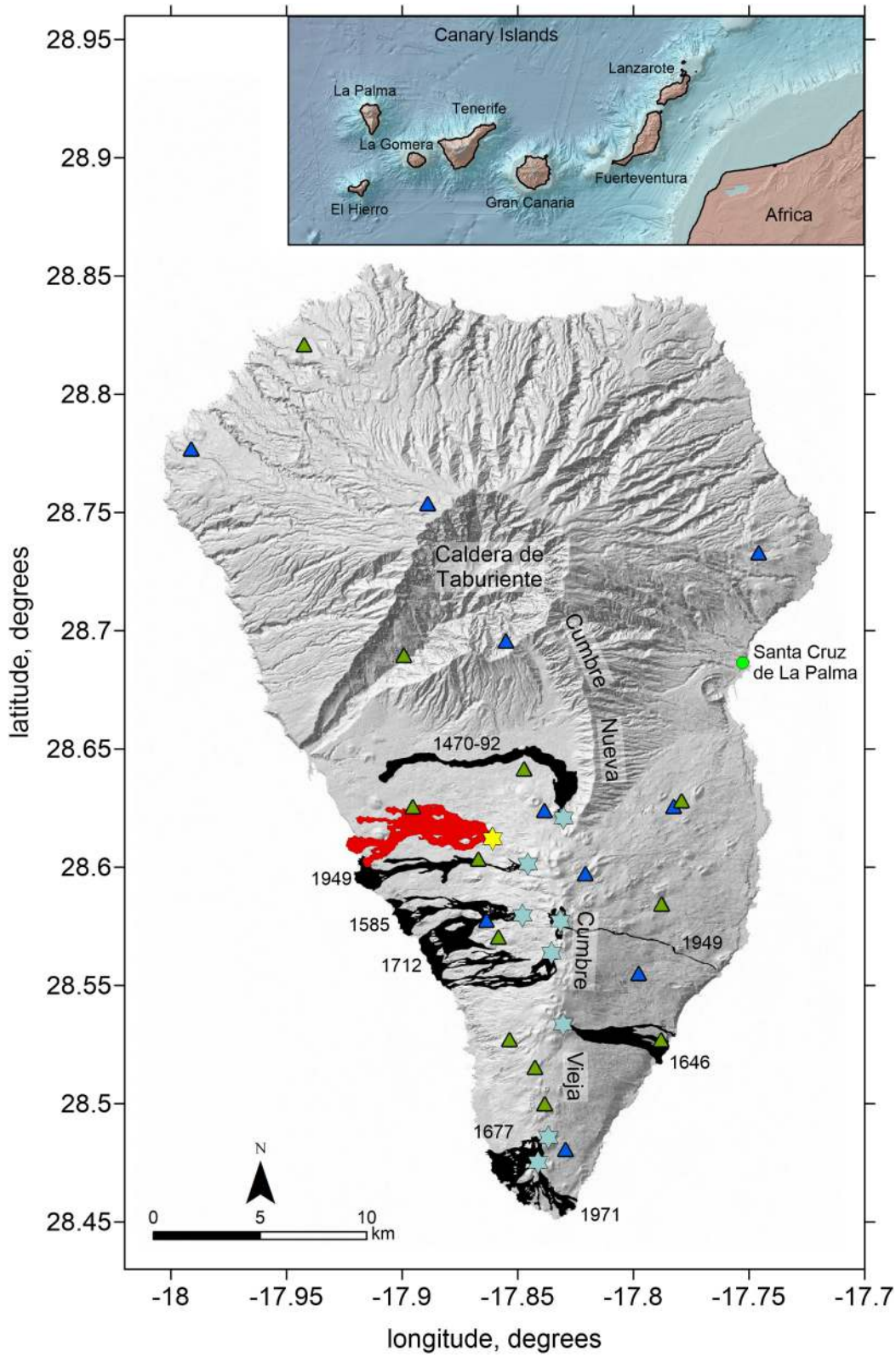

Figure 1. Topography map of La Palma Island with the locations of seismic networks INVOLCAN (green triangles) and IGN (blue triangles). Black shading denotes lava flows from historical eruptions with the indications of years, and red shading denotes lava flows from the 2021 eruption. The light-blue stars indicate historical eruption vents, and the yellow star is the vent of the 2021 eruption. Inset is the map of Canary Islands.

typically exhibit gradual, prolonged activity over months or years. Third, unlike previously studied volcanoes, which were primarily associated with subduction zones and characterized by moderately explosive eruptions of high-viscosity felsic magma, La Palma is a hotspot volcano with a predominantly effusive eruption style. The exceptionally high volume of erupted basaltic lava and gases suggests that underground processes at La Palma may differ significantly from those observed in subduction-related volcanoes.

By applying repeated tomography to this unique case, we aim to uncover new insights into the underground processes that drive large effusive eruptions—insights that may not have been evident in previous studies of other volcanic systems.

2. Geological Settings of La Palma and the 2021 Cumbre Vieja Eruption

La Palma is one of the islands of the Canary archipelago located in the Atlantic Ocean off the northwest coast of Africa that is a prime example of hotspot volcanism (inset in Figure 1). The Canary Islands are located on a passive continental margin, approximately 100 km west of the northwest African coastline. Their formation is attributed to a mantle plume or a deep-seated upwelling of hot material from the Earth's mantle, which has been active for at least 70 million years (Carracedo et al., 1998). This plume interacts with the overlying lithosphere, creating a chain of volcanic islands as the African Plate slowly moves northeastward over the stationary hotspot (Geldmacher et al., 2005).

The archipelago consists of seven main islands (inset in Figure 1)—Tenerife, Gran Canaria, Lanzarote, Fuerteventura, La Palma, La Gomera, and El Hierro—each showcasing unique volcanic landscapes, ranging from towering stratovolcanoes to expansive lava fields. While the oldest islands, such as Fuerteventura and Lanzarote, date back over 20 million years, the youngest, like Tenerife, El Hierro and La Palma are still experiencing geological activity, including seismic swarms and occasional eruptions (Guillou et al., 2001). This age progression aligns with the movement of the African Plate, consistent with the hotspot model. However, the Canary Islands also display anomalies, such as the simultaneous activity on multiple islands, suggesting additional factors like lithospheric fractures or edge-driven convection may influence volcanism (Anguita & Hernán, 2000).

La Palma, the fifth-largest island in the Canary archipelago, is one of the most geologically active and dynamic volcanic islands in the world. Formed approximately 1.8 million years ago, it is the second youngest island in the chain and is characterized by its dramatic topography related to volcanic activity (Carracedo et al., 2001). Its structure is characterized by two main volcanic formations (Figure 1): the older, deeply eroded northern region, marked by the Caldera de Taburiente, and the younger, more active southern region, dominated by the Cumbre Vieja volcanic ridge (Carracedo & Troll, 2016). The hot spot volcanism has resulted in a diverse range of volcanic features, including basaltic lava flows, cinder cones, and explosive eruptions, making La Palma a key site for studying volcanic processes and hazards. La Palma's geology is also influenced by gravitational collapses, as seen in past landslides that have affected its western flank (Masson et al., 2002).

La Palma has experienced several historical eruptions, primarily concentrated along the Cumbre Vieja volcanic ridge, which is the island's most active geological feature (Figure 1). Since the Spanish colonization of the Canary Islands in the 15th century, at least seven eruptions have been recorded. The first well-documented eruption occurred in 1,470–1,492, known as the Tacande eruption, which formed the Montaña Quemada cinder cone and produced extensive lava flows that reached the western coast (Carracedo et al., 2001). Another notable eruption took place in 1,585, when the Tajuya volcano erupted, generating lava flows that destroyed farmland and settlements (Hernández-Pacheco & Valls, 1982). Subsequent eruptions followed in 1,646 (Tigalate), 1,677–1,678 (San Antonio), and 1,712 (El Charco), each contributing to the island's expanding landmass with lava flows that reached the ocean. The San Juan eruption in 1949 was particularly notable, as it produced three main eruptive vents—Duraznero, Llano del Banco, and Hoyo Negro—and resulted in significant lava flows (Hernández-Pacheco & Valls, 1982). The last eruption before the 21st century in 1971 at Teneguía lasted 24 days and was characterized by Strombolian activity, lava flows, and the emission of volcanic gases (Carracedo et al., 2001). While it caused minimal damage due to its location near the island's southern coast, it provided valuable insights into the island's ongoing volcanic activity.

The 2021 eruption of La Palma was one of the most significant volcanic events in the Canary Islands' recent history. It began on 19 September 2021, when a fissure opened on the western flank of the Cumbre Vieja volcanic ridge, releasing lava fountains and ash plumes. The eruption was preceded by weeks of seismic activity and

ground deformation, indicating magma intrusion beneath the island (Carracedo et al., 2022; Torres-González et al., 2022). Over the course of 85 days, the eruption produced extensive lava flows that covered approximately 1,200 ha, destroying thousands of homes, roads, and agricultural land (González-de-Vallejo et al., 2024). The lava reached the Atlantic Ocean in late September, forming new land through the accumulation of solidified lava deltas, or "fajanas," along the coastline. Volcanic ash and gases, including sulfur dioxide (SO_2), caused air quality concerns and affected local communities (Romero et al., 2022). The eruption finally ended on 13 December 2021, after nearly 3 months of activity. While no direct fatalities were reported, the economic and environmental impacts were substantial, with damages estimated in the billions of euros.

Recent studies on the 2021 eruption of Cumbre Vieja have provided valuable insights into its geological, petrological, and geochemical characteristics. Geochemical analyses of the erupted materials revealed relatively uniform compositions, with subtle variations over time. These findings suggest that the magma chamber experienced discrete injections of new magma during the eruption, influencing the eruption's dynamics (Torres-González et al., 2022). Petrological investigations have identified the presence of CO_2-rich fluid inclusions within erupted minerals, indicating that the main magma reservoir was located at significant depths beneath the island. This deep storage allowed for the accumulation of volatiles, which played a crucial role in driving the explosive phases of the eruption (Amonte et al., 2022).

Seismic tomography studies have significantly advanced our understanding of the subsurface structure and magmatic processes beneath La Palma, particularly in relation to the 2021 eruption of the Cumbre Vieja volcano. A notable study by D'Auria et al. (2022) employed seismic tomography to investigate the magmatic system beneath La Palma. Their findings revealed a substantial magma storage region and evidence of rapid magma ascent from the base of the oceanic crust to the surface, culminating in the 2021 eruption. This rapid ascent underscores the dynamic nature of the magmatic processes at play. Further research by Serrano et al. (2023) utilized local earthquake data to construct a detailed 3D anisotropic model of the crust beneath La Palma. The distributions of anisotropic parameters provide insights into crustal heterogeneity, stress fields, and magmatic pathways. A recent study by Cabrera-Pérez et al. (2024) introduced an Ambient Noise Attenuation Tomography technique to image the 3-D intrinsic attenuation structure of La Palma. This method leverages ambient seismic noise to identify anomalies that may be associated with active geothermal reservoirs, highlighting areas with potential geothermal energy resources. Syn-eruptive analyses have also been conducted to monitor fluid migration within the volcanic edifice. Cabrera-Pérez et al. (2023) applied ambient noise correlation analyses to detect temporal changes in seismic velocities. These changes are generally associated with variations in the stress field and fluid movements.

These geophysical studies not only enhanced our understanding of the eruption's subsurface dynamics but also contributed to refining volcanic hazard models and improving early warning systems for future eruptions. The 2021 La Palma eruption was a landmark geological event, providing valuable insights into hotspot volcanism and early warning methodologies.

3. Data and Method

To investigate the crustal structure beneath La Palma, we utilized travel time data recorded by 11 stations from the Instituto Geográfico Nacional (IGN) and 12 stations from the Instituto Volcanológico de Canarias (INVOLCAN) (Figure 1). These stations were operational before, during, and after the eruption. All stations were equipped with three-component broadband seismometers, recording seismic signals at a sampling rate of 100 Hz.

It is important to note that IGN and INVOLCAN conducted their monitoring independently, employing different methodologies, which resulted in slightly varying solutions for earthquake hypocenters and origin times. To address this, we initially merged the data sets from both agencies by applying a criterion that the origin times should not differ by more than 1 s and that hypocenter locations should be close (less than 3 km of difference). The combined data set used in this study comprised 13,681 seismic events, with 140,078 P-wave and 155,231 S-wave picks.

The time-depth distribution of these events is presented in Figure 2. The upper panel shows that prior to the seismic activation in September 2021, several episodic swarms occurred, predominantly at depths between 10 and 20 km, and rarely extending to 25 km. Notably, almost no shallow seismicity was observed in this period. As highlighted in the lower panel of Figure 2, a significant change began on 11 September 2021, with seismicity

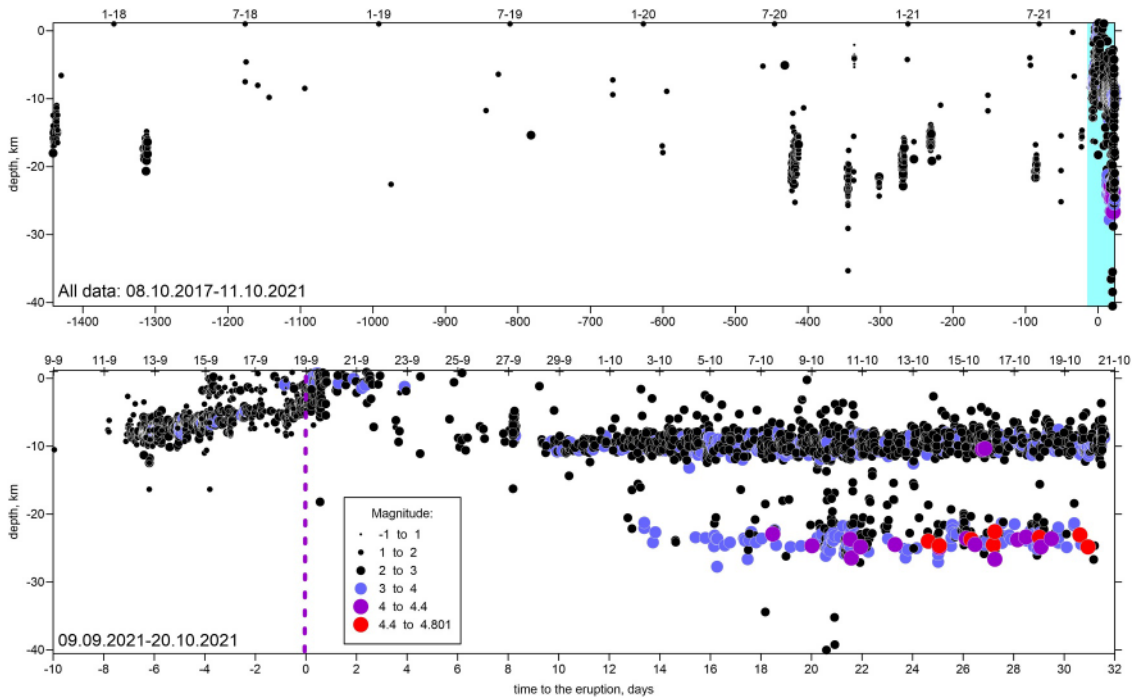

Figure 2. Distribution of seismicity beneath La-Palma Island depending on depth and time. The upper plot shows the entire observation period, whereas the lower plot presents the seismicity associated with the Cumbre Vieha eruption in 2021 highlighted by the blue band. The events are classified according to the magnitudes using different colors and sizes of symbols. The dotted line indicates the moment of the eruption beginning.

initiating at depths of 7–10 km. Over the following week, the seismicity migrated upwards, culminating at the surface with the eruption onset on 19 September 2021. Following the eruption's start, shallow seismicity persisted for only 2–3 days before ceasing. A prominent seismicity cluster emerged around 10 km depth 9 days after the eruption began and continued actively until the eruption's end. A second cluster, characterized by higher magnitude earthquakes, initiated 13 days post-eruption at depths of 20–25 km. The existence of seismicity across a broad depth range provides favorable conditions for local earthquake tomography. This data set was previously employed by D'Auria et al. (2022) to construct a comprehensive 3D tomography model of La Palma spanning the entire period before and during the eruption. In our study, this extensive data set enables the optimal selection of paired events from distinct time intervals, which is crucial for our repeated tomography approach aimed at isolating temporal changes in velocity structure. The extensive number of events in the data set allows for optimal data selection across different time intervals, ensuring both sufficient consistency and high-density ray coverage for robust analysis.

The tomographic inversion was performed using the LOTOS code (Koulakov, 2009), a well-established tool that has been applied to study numerous volcanoes worldwide (e.g., Bushenkova et al., 2019; Kasatkina et al., 2022; Koulakov et al., 2021; Yaroshenko et al., 2022), including La Palma (D'Auria et al., 2022). The inversion process begins with the preliminary location of all seismic sources from the catalog within a starting 1D velocity model, identical to the one used by D'Auria et al. (2022). At this initial stage, we filtered the data by excluding events with residuals exceeding 0.5 s for P-wave picks and 0.7 s for S-wave picks, as well as events with fewer than eight picks.

In this study, we conducted repeated tomography inversions to investigate changes in the velocity structure before and after the onset of the eruption on La Palma on 19 September 2021. For each inversion, we selected paired data sets corresponding to pre- and syn-eruption time intervals. To assess the stability of the detected velocity changes, we systematically varied the cutoff dates for the first data set (pre-eruption) and the start dates for the second data set (syn-eruption). In our primary model, the first data set spanned from 8 October 2017 to 19 September 2021, while the second data set covered the period from 24 September 2021 to 15 December 2021.

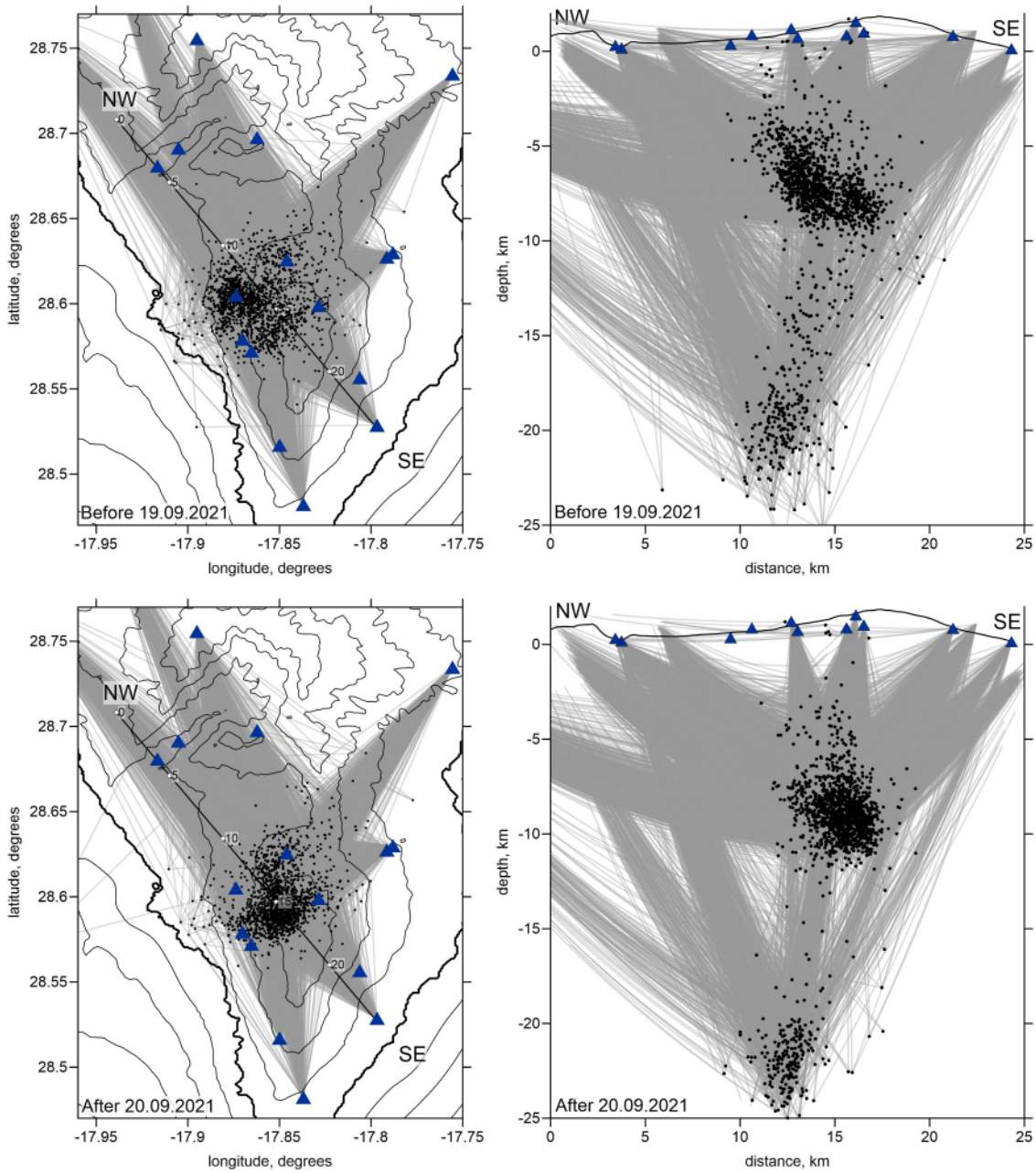

Figure 3. Distribution of seismic data before 19.09.2021 (upper row) and after 20.09.2021 (lower row), displayed in map view (left column) and vertical profile (right column). Black dots indicate event locations after the first iteration, blue triangles represent seismic stations, and gray lines denote P-wave ray paths. In the vertical profile, events and ray paths are plotted within 5 km of the profile line. The black line in the profile corresponds to the topographic relief along the section. Topography in the maps is represented by contour lines at 200 m intervals.

For the two time windows, we ensured an identical number of events in each data set, with each event in the first data set paired to an event in the second data set located within a distance of less than 3 km (Figure 3). From all possible event pairs, we selected those with the maximum number of common stations and identical P- and S-wave phases. A minimum of six common phases was required for each pair of events. As a result, the final data sets contained equal numbers of events, P- and S-wave phases, and exhibited similar spatial distributions of ray paths, as demonstrated in Figure 3. The exact numbers varied depending on the chosen end time of the first data set and the start time of the second data set.

For the main model, corresponding to the time windows of 8 October 2017 to 19 September 2021 (pre-eruption) and 20 September 2021 to 15 December 2021 (syn- and post-eruption), we selected 1,528 events, comprising 13,089 P-wave picks and 13,870 S-wave picks, averaging 17.6 picks per event. It is important to note that the number of rays in our study is significantly lower than that used by D'Auria et al. (2022), resulting in a lower resolution for our tomographic models compared to their results. However, our primary focus is on analyzing temporal changes in the velocity structure rather than achieving high spatial resolution.

The selected data sets were independently inverted using the LOTOS tomography code (Koulakov, 2009). The complete structure of the code, along with all data sets, is available at Zenodo (Koulakov, 2025) and can be used to reproduce the results presented in this study. For all models, we employed the same 1D starting reference model previously derived by D'Auria et al. (2022) for the tomographic inversion of the full data set. This reference model was also used for the preliminary location of seismic sources in the entire catalog prior to the selection of data subsets. As a result, no data were excluded during the repeated tomography process, ensuring that the paired data subsets maintained identical numbers of events and rays throughout the procedure.

The iterative inversion procedure consists of several key steps: determining source locations within the 3D models, calculating the sensitivity matrix, and performing the inversion. The source location algorithm utilizes the bending method for ray tracing, which identifies ray paths with minimum travel times. The point of highest source probability is determined using a gradient descent method.

The 3D velocity models were parameterized using nodes distributed throughout the study volume based on data availability. The horizontal grid spacing was set to 0.7 km. In the vertical direction, the spacing varied depending on ray density: it was 0.7 km in regions with high ray sampling and increased in areas with lower ray density. Nodes were not placed in regions without ray coverage. The total number of parameter nodes was approximately 3,000 for the P-wave model and 3,200 for the S-wave model. To ensure grid independence in the solutions, we performed inversions using rotated grids with basic orientations of 0°, 22°, 45°, and 66°. The results from these multiple grids were averaged into a regularly spaced velocity model, which served as the reference model for the subsequent iteration. The parameterization grid was constructed only during the first iteration; in later iterations, the model was updated using the same node configuration. For the repeated tomography inversions in two time episodes, the grid was created for the first episode and then replicated for the model corresponding to the second episode.

The inversion was carried out simultaneously for the source and velocity parameters using the least squares method with QR decomposition, specifically the LSQR algorithm (Nolet, 1987; Paige & Saunders, 1982). The stability of the solution was ensured by incorporating regularization matrices that impose amplitude damping and smoothing constraints. The values of the corresponding control parameters were optimized based on the results of synthetic tests. For all time episodes, we used identical sets of inversion parameters, including smoothing factors of 0.3 and 0.8 for P- and S-wave velocity anomalies, respectively, and corresponding amplitude damping factors of 0.3 and 0.8.

To evaluate the sensitivity of our results to the choice of regularization, we performed inversions with significantly different damping parameters. Figure S3 in Supporting Information S1 shows examples of an underdamped solution (smoothing and amplitude factors of 0.2 and 0.5 for the P- and S-wave models, respectively) and an overdamped solution (factors of 0.5 and 1.3, respectively). While the absolute amplitudes of the Vp and Vs anomalies vary significantly with different damping, the key observation is that the spatial patterns of the main structures, and consequently the resulting Vp/Vs ratio anomalies central to our interpretation, remain robust and stable.

The iterative inversion procedure inherently addresses the potential coupling, or trade-off, between source locations and velocity structure—a crucial consideration when comparing models from different time periods. For each time interval (pre- and syn-eruption), the inversions were performed independently. Within each iteration, source locations were updated twice: first during the simultaneous inversion for P- and S-wave velocities, and again in a dedicated relocation step using the newly updated 3D model. This period-specific, iterative relocation ensures that hypocenters are consistently optimized within the updated velocity structures, minimizing systematic location biases that could otherwise obscure genuine temporal changes.

In this study, we primarily focus on analyzing the Vp/Vs ratio, as it is the most sensitive parameter for detecting the presence of fluids and melts within the magma feeding system. In our algorithm, the Vp/Vs ratio was

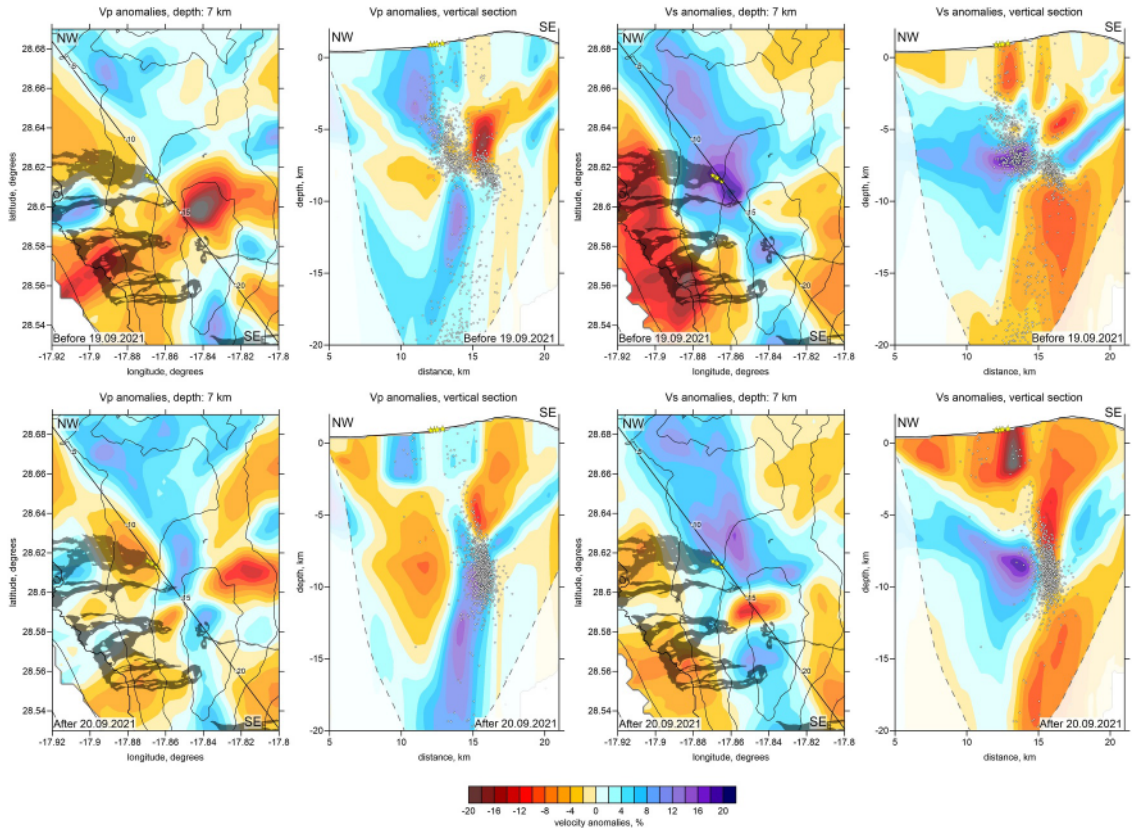

Figure 4. Anomalies of Vp and Vs in horizontal and vertical cross-sections for two time intervals: before 19.09.2021 (upper row) and after 20.09.2021 (lower row). Topography in the maps is represented by contour lines at 200 m intervals. Dark zones indicate lava flows from historical eruptions, and yellow stars mark the vents of the 2021 eruption. Dots indicate the seismicity within 3 km interval from the section. Non-resolved areas in vertical sections are blanked with semi-transparent areas.

calculated by directly dividing the derived absolute P- and S-wave velocities. Given that the number of P- and S-wave picks was nearly identical, the resolution of both models was comparable, ensuring the stability of the velocity ratio. To further validate the robustness of the Vp/Vs ratio determination, we conducted a series of synthetic tests in which this parameter was calculated in the same manner as in the experimental data inversion.

4. Results of Real and Synthetic Data Inversions

The resulting distributions of Vp and Vs anomalies for the two time windows (8 October 2017 to 19 September 2021 and 24 September 2021 to 15 December 2021) are displayed in one horizontal and one vertical section in Figure 4. The corresponding Vp/Vs ratios, which were obtained by division of the absolute P and S wave velocities, are presented in Figure 5. In the horizontal section at 7 km depth below sea level (b.s.l.), a large area of low Vp/Vs ratio is observed in the central part of the study region. During the first time window, this anomaly spans the entire central area, while in the second time window, a distinct isometrical anomaly of high Vp/Vs ratio emerges, coinciding with a cluster of seismicity.

In the vertical section, the first time interval reveals prominent high Vp/Vs anomalies separated by a layer of low Vp/Vs ratio located between 5 and 8 km depth b.s.l. (upper-right panel in Figure 5). In contrast, during the second time window, a vertically oriented high Vp/Vs anomaly is observed, connecting the shallow and deep anomalies (lower-right panel in Figure 5). We interpret this feature as a magma conduit that formed during the onset of the eruption on 19 September 2021 and subsequently facilitated the transport of significant volumes of magma over the nearly 3-month duration of the eruption.

To assess the stability of the magma conduit image and its potential evolution over time, we conducted a series of inversions with varying time window limits. In Figure 6, we kept the first time interval (8 October 2017 to 19 September 2021) unchanged while adjusting the start of the second interval from 20 September 2021 to 20

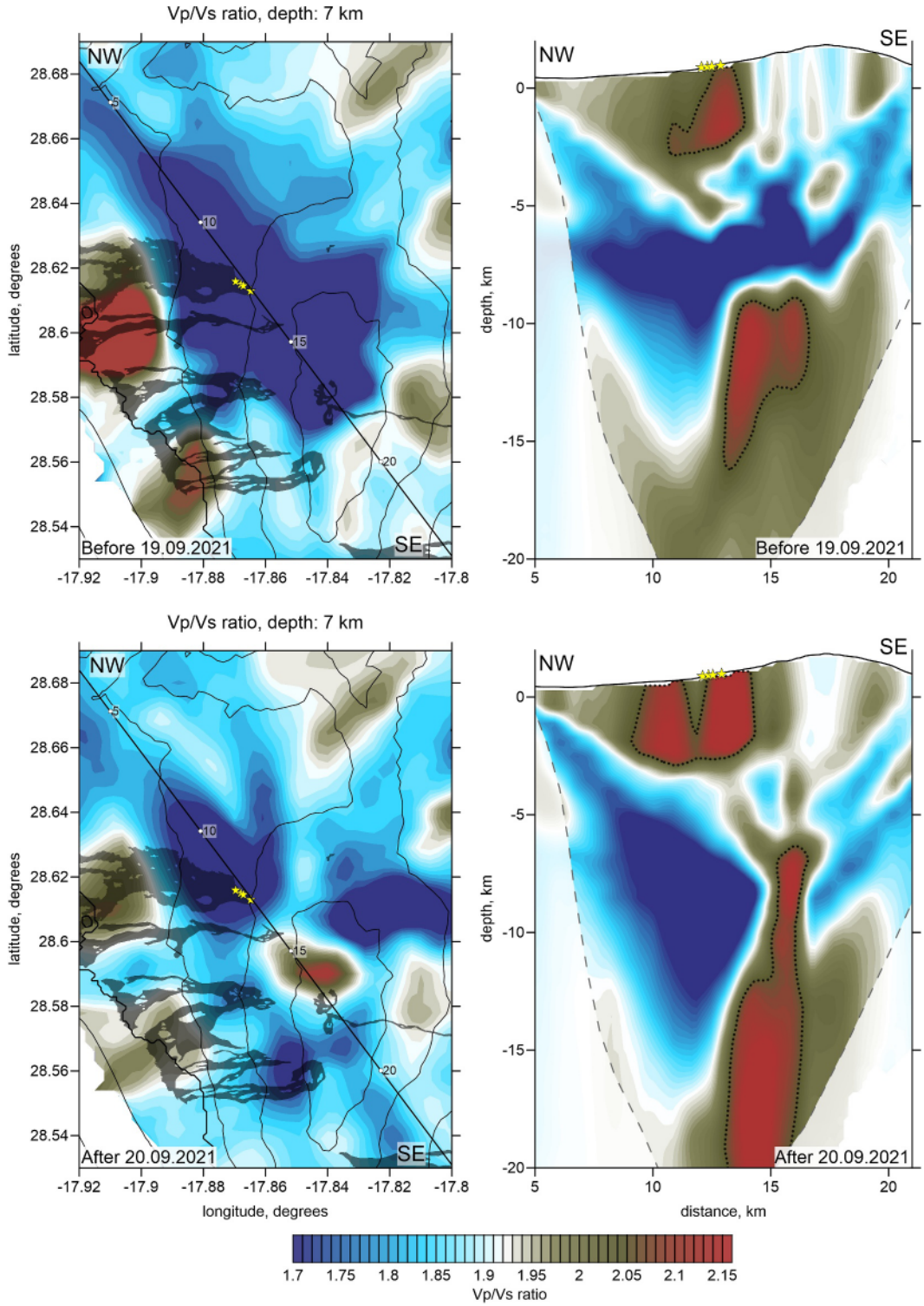

Figure 5. Distribution of the Vp/Vs ratio in horizontal and vertical cross-sections for two time intervals: before 19.09.2021 (upper row) and after 20.09.2021 (lower row). Topography in the maps is represented by contour lines at 200 m intervals. Dark zones indicate lava flows from historical eruptions, and yellow stars mark the vents of the 2021 eruption. Dotted line in vertical sections indicate the contour line of Vp/Vs = 2.05. Non-resolved areas in vertical sections are blanked with semi-transparent areas.

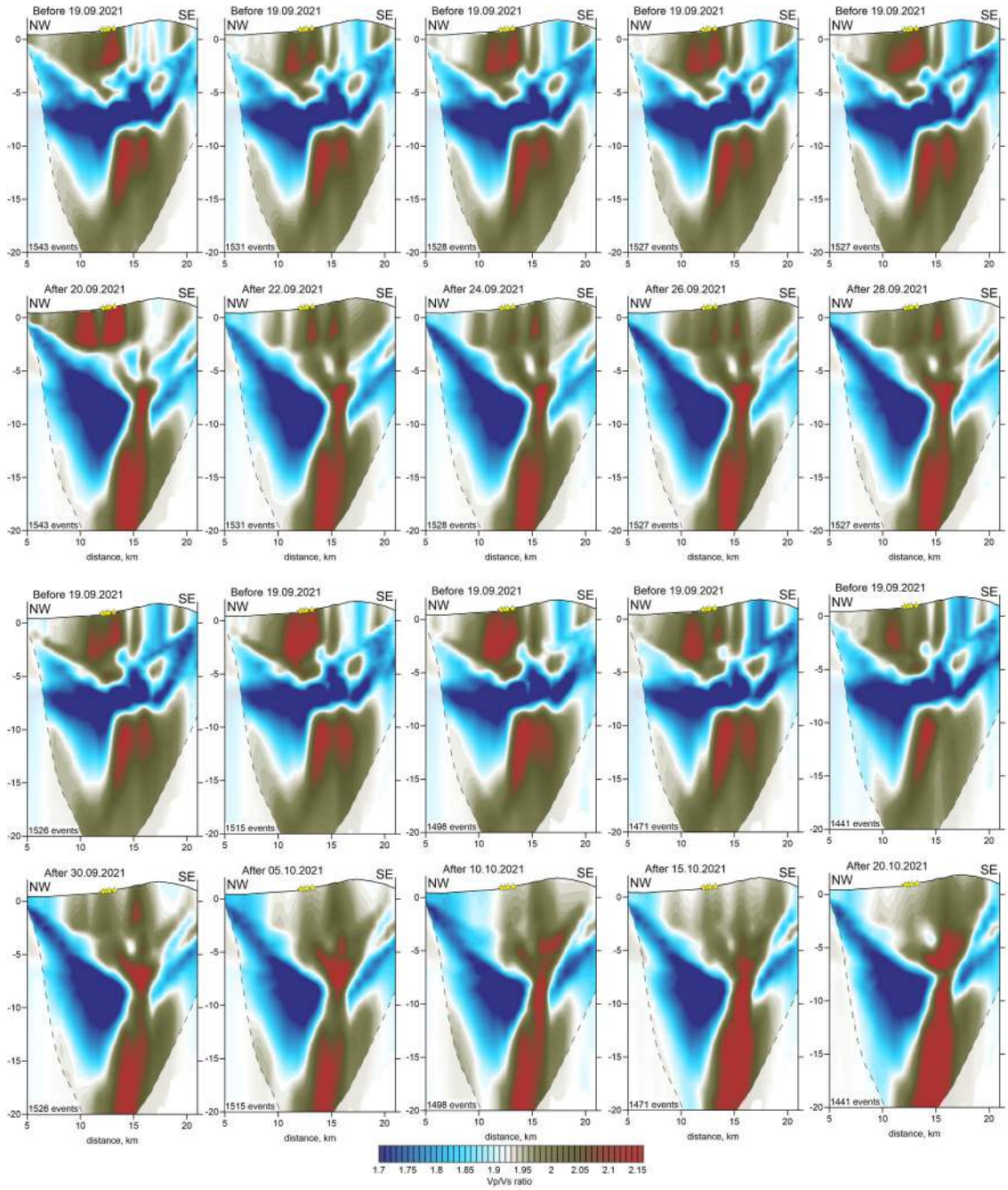

Figure 6. Distribution of the Vp/Vs ratio in vertical cross-sections for different time intervals. The first interval remains unchanged (before 19.09.2021), while the start of the second interval varies (from 20.09.2021 to 20.10.2021). Data were selected to ensure identical numbers of rays and similar distributions. Variations in the time range of one interval affect the corresponding data set, leading to changes in the tomography models for both intervals. The numbers of events are indicated in each panel.

October 2021. The distributions of seismicity corresponding to 10 pairs of data subsets in selected time intervals are shown in Figure S1 in Supporting Information S1. Theoretically, since the first time interval remains constant, the corresponding structures should also remain unchanged. However, in practice, for each pair of data subsets, we select data with similar ray configurations. Consequently, as the time-limits of the second data set are adjusted, the distribution of events changes in both data sets, leading to some variations in the structures of both models. In the cases shown in Figure 6, the changes in the first data set remain relatively small. For the second data set, in all inversion results, we observe a vertical anomaly of high Vp/Vs ratio, which is interpreted as a magma conduit. We

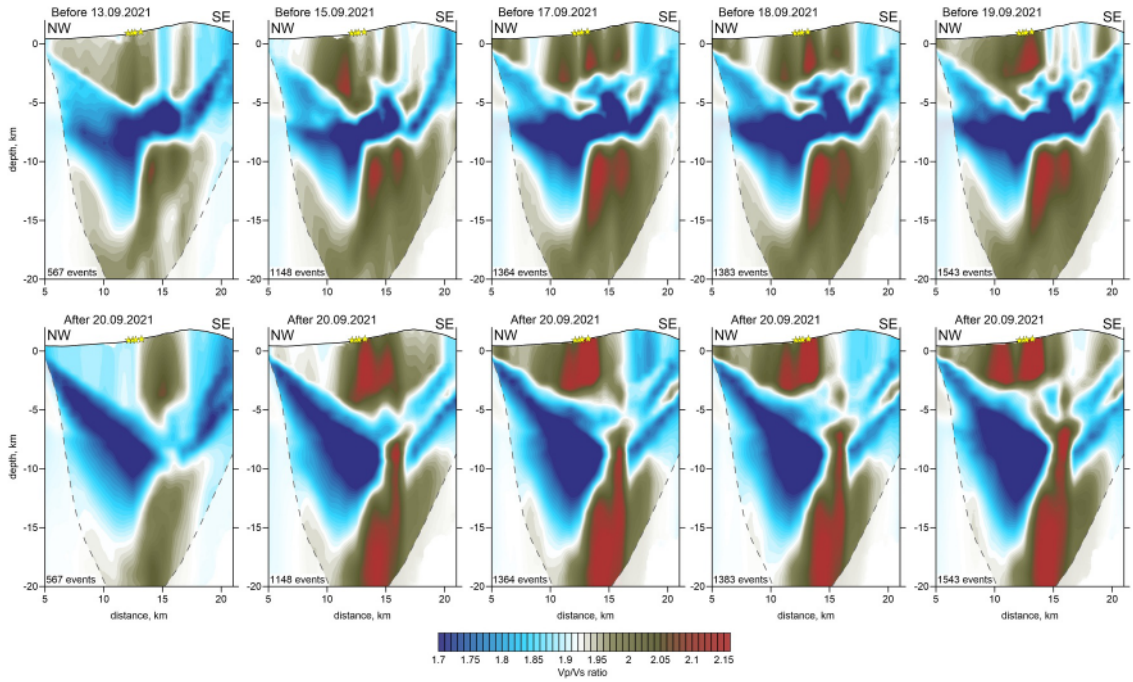

Figure 7. Same as Figure 6, but here the start of the second time interval remains unchanged, while the end of the first interval is varied. Shifting the date to an earlier time results in a significant reduction in data volume, leading to a loss of resolution in the tomography models. The numbers of events are indicated in each panel.

can see a gradual evolution in the shape of this anomaly. For cases where the second interval begins before 28 September 2021, the top of the conduit remains at an unchanged depth of approximately 6 km b.s.l., while the head of the plume becomes more pronounced. After 30 September 2021, the head of the plume begins to ascend, forming a large anomaly within the depth range of 4–7 km b.s.l. It is important to note, however, that these apparent changes do not directly reflect the real-time evolution of subsurface structures. This is because the data corresponding to earlier stages incorporate all factors over the entire time interval, whereas models with later start dates exclude earlier influences.

In Figure 7, we present a test similar to that in Figure 6, but in this case, we kept the start time of the second data set unchanged while varying the end time of the first data set from 13 September 2021 to 19 September 2021. The corresponding distributions of events in five time intervals are presented in Figure S2 in Supporting Information S1. Unlike the first data set, the number of events in this case decreases significantly as the end time is shifted earlier. For example, when the first data set ends on 19 September 2021, we obtained 1,543 events for both data sets, whereas for the case ending on 13 September 2021, only 567 events were selected. Consequently, the resolution for the 13 September 2021 case is expected to be considerably lower compared to the 19 September 2021 case, due to poorer data coverage in both subsets.

A potential concern is that the observed changes in the velocity models might be influenced by imperfect alignment of event distributions between the data sets, as seen in Figure 3 and in Figures S1–S2 in Supporting Information S1. Specifically, the distances between paired events can be up to 3 km, which may introduce significant variations in ray path coverage that could affect the results of the repeated tomography.

To address this concern, we conducted a series of synthetic tests designed to simulate the realistic workflow of repeated tomography. An important aspect of these tests was to honestly account for the source-velocity trade-off inherent to local earthquake tomography. In these tests, we defined three-dimensional synthetic anomalies for Vp and Vs, using either checkerboard patterns or polygons representing realistic structural shapes. Based on these synthetic models, we calculated synthetic travel times using the bending algorithm for ray tracing, incorporating the actual distributions of source-receiver pairs from the same data subsets as used for the analysis of experimental data. The computed synthetic times were perturbed with Gaussian random noise, with mean deviations of 0.03 s for P-waves and 0.05 s for S-waves. To simulate realistic uncertainty in earthquake locations, the initial hypocenter locations for the synthetic data were intentionally perturbed randomly from their true positions, with mean

shifts of ∼3 km. We then initiated the recovery procedure using the same workflow and control parameters as in the experimental data inversion, including the step of grid-search source localization within the 1D reference model and subsequent iterative joint inversion for velocities and locations. This approach ensures that our synthetic tests evaluate whether key structures can be reliably resolved despite the coupling between source parameters and velocity structure.

Figure S4 in Supporting Information S1 presents the results of a checkerboard resolution test for a model defined in map view. The synthetic model contains positive and negative anomalies with an amplitude of ±8% for Vp and Vs, respectively, with reverse polarities to generate strong contrasts in the Vp/Vs ratio. The anomalies are 2.5 km in size, separated by 1 km intervals. The recovery was performed using the actual source-receiver configurations from our two main time intervals: before (8 October 2017 to 19 September 2021) and during the eruption (20 September 2021 to 15 December 2021). The results show that anomalies of this scale are robustly recovered across most of the study area for both periods, demonstrating adequate horizontal resolution.

It is well-established that vertical resolution in local earthquake tomography is generally poorer than horizontal resolution due to the fundamental problem of the trade-off between source location parameters and velocity distributions. To evaluate this, we performed a vertical checkerboard test (Figure S5 in Supporting Information S1), using the same cross-section as for the main results. The synthetic model consists of rectangular anomalies with amplitudes of ±8%, measuring 2.5 km horizontally by 3.5 km vertically, and separated by 2 km intervals. As in the previous case, the Vp and Vs anomalies were assigned opposite signs to produce strong Vp/Vs variations. The recovery, performed with the same data subsets as the previous test, shows some vertical smearing, as expected. Despite this, the core positions and overall configuration of the synthetic anomalies are successfully retrieved in both time intervals, indicating that the major vertical structures we interpret are robustly resolved.

To further investigate the potential influence of source clustering on the appearance of conduit-shaped anomalies, we designed an additional series of tests, the results of which are presented in Figure 8. In this case, we created two free-form models representing realistic configurations of the Vp/Vs ratio: one with a conduit and one without (shown in the left column of Figure 8). These structures were derived by separate definition of the Vp and Vs anomalies, as shown in the left column in Figure 8. These synthetic models were then recovered using data configurations corresponding to the time intervals before 19 September 2021 and after 20 September 2021 (middle and right columns, respectively). The recovery results for both types of synthetic models are remarkably similar, demonstrating that the observed changes in the experimental data cannot be attributed to uneven data distributions. Instead, they genuinely reflect real variations in seismic velocities caused by processes within the volcanic plumbing system during the eruption. This test also shows that the inversion is capable of resolving localized conduit-related anomalies of approximately 1 km thick in the well-sampled central part of the study area.

To rigorously assess whether the temporal evolution of the conduit imaged in Figure 6 is real or an artifact of changing ray coverage, we performed synthetic recovery tests for all paired data subsets used in that analysis. Figure S6 in Supporting Information S1 shows the recovery of Model 1 (without a conduit) across the 10 different time intervals, while Figure S7 in Supporting Information S1 shows the recovery of Model 2 (with a conduit). The results demonstrate that while a loss of shallow resolution occurs when later intervals exclude the initial post-eruption shallow seismicity, the conduit in Model 2 is consistently and robustly restored in all cases. Crucially, the recovery of Model 1 never produces a false conduit. Therefore, the temporal changes observed in the experimental results (Figure 6)—specifically the emergence and evolution of the high Vp/Vs anomaly—are required by the data and represent genuine subsurface changes, not variations in ray path configurations.

Finally, we applied the same synthetic tests to the five data subsets where the start of the later interval was fixed and the end of the earlier interval was varied (Figure 7). The results for both Models 1 and 2 are shown in Figure S8 in Supporting Information S1. For the subset ending on 13 September 2021, which has significantly fewer events, the recovery models show a pronounced loss of amplitude and spatial resolution. This degradation directly correlates with the poorer data coverage. Therefore, the apparent loss of structural definition in the experimental results for the earliest cutoff (Figure 7) is most likely an artifact of the sparser ray sampling and does not reflect a genuine physical change in the subsurface.

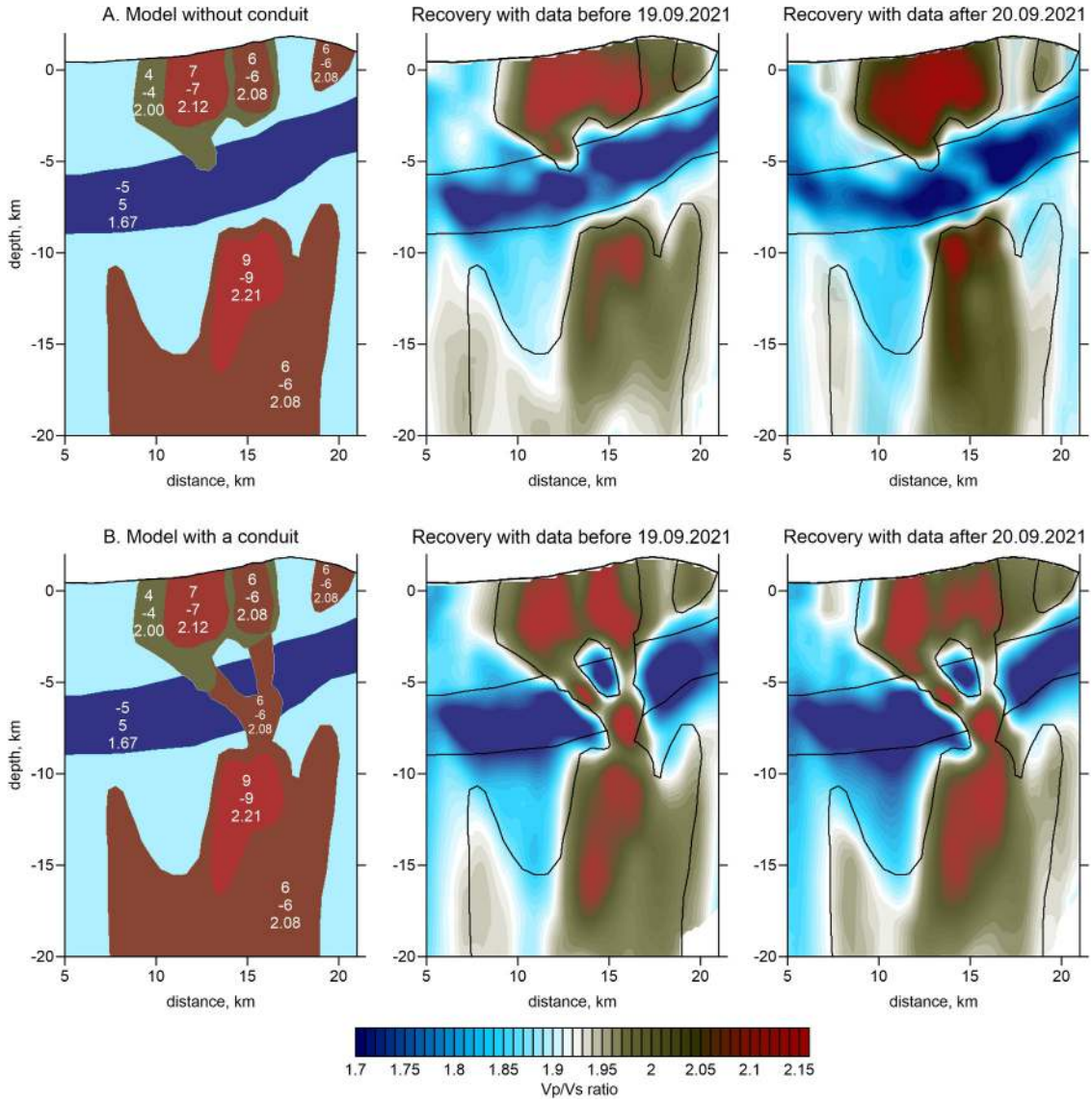

Figure 8. Synthetic tests with realistic structures of the Vp/Vs ratio in vertical cross-sections. Two models are considered: one with a conduit and one without. Recovery of both models is performed using data sets corresponding to the time intervals before 19.09.2021 and after 20.09.2021. The left column shows the initial synthetic models, while the middle and right columns display the recovery results. In the resulting images, the initial synthetic anomalies are highlighted with black contour lines. The numbers on synthetic anomalies in the left column indicate the values of dVp, dVs (in percent) and the corresponding Vp/Vs ratio.

5. Discussions

The structures of the P- and S-wave velocity anomalies shown in Figures 4 and 5 are generally consistent with the tomography model derived by D'Auria et al. (2022), which is expected as we used the same algorithm (slightly adapted for repeated tomography). In our case, the models appear less contrasted and contain fewer details due to the lower resolution resulting from the smaller data sets used for inversions.

Our model can also be compared with the results of Serrano et al. (2023), who obtained 3D distributions of Vp and the Vp/Vs ratio using the same data set but an alternative local earthquake tomography algorithm. Their model shows a prominent anomaly of low Vp and low Vp/Vs ratio directly beneath the eruption vents at 7 km depth, which is consistent with our findings. Furthermore, at a depth of 9 km to the south of the vent, they observe a local high Vp/Vs anomaly, corresponding with the location of the conduit imaged in our study during the eruption.

Our work is also consistent with the temporal seismic velocity variations derived from ambient noise data by Cabrera-Pérez et al. (2023). They identified a zone, located to the south of the future vent, that exhibited a gradual decrease in seismic velocity in the days before the eruption onset. This temporal velocity reduction may correspond to the initial stages of the magma conduit's ascent, as identified in our repeated tomography.

Finally, our results can be compared with the ambient-noise attenuation tomography of Cabrera-Pérez et al. (2024). The most prominent feature in their model is a clear separation between high attenuation down to ∼2 km depth and low attenuation in deeper sections below the Cumbre Vieja ridge and vent. This feature is highly consistent with the distribution of the Vp/Vs ratio in our study, which shows very high values at shallow depths in the same area. If we consider that the primary cause of a high Vp/Vs ratio is high fracturing and fluid saturation, it is natural that the same factors would also cause increased seismic wave attenuation.

As can be seen in the vertical section in Figure 4, the Vp anomaly in our model is dominated by a high-velocity column beneath the vents of the 2021 eruption, which is observed in both time intervals. In contrast, the Vs anomaly model exhibits predominantly low velocities in approximately the same locations. This inverse correlation between P- and S-wave velocity anomalies is a common feature observed beneath many active volcanoes (e.g., Bushenkova et al., 2019; Kasatkina et al., 2022; Koulakov et al., 2021; Vargas et al., 2017). As demonstrated by numerous physical experiments on various rock types, P-wave velocity is primarily sensitive to rock composition (e.g., Lin et al., 2015; Shearer, 1988). Zones of basaltic intrusions typically exhibit high P-wave velocities, a characteristic that holds true for both fully consolidated and partially molten rocks. In contrast, S-wave velocity is less sensitive to composition and is more strongly influenced by the presence of liquid phases, such as partial melts or fluids within pores (e.g., Kuster & Toksoz, 1974; Shearer, 1988; Takei, 2002).

In this context, the distribution of the Vp/Vs ratio is particularly informative, as it is highly sensitive to the presence of melts and volatiles. Figure 5 illustrates the changes in the Vp/Vs ratio between the two time episodes in our main model, displayed in one horizontal and one vertical section. In both time intervals, the shallow structures near the vents of the 2021 eruption are dominated by a high Vp/Vs ratio, suggesting the presence of liquids at depths of up to ∼3 km below the surface. Prior to the 2021 eruption, there was no significant volcanic or geothermal activity in this area (e.g., Carracedo et al., 2001), implying that these anomalies may reflect rock saturation by meteoric fluids.

Following the onset of the eruption, the intensity of the shallow high-Vp/Vs anomalies decreased slightly. Interpreting this change is complex, as it may result from a combination of factors. A plausible physical contributor could be the vapourization of meteoric fluids by the ascending magma, which would generate steam and lower the Vp/Vs ratio (Husen et al., 2004; Kuznetsov et al., 2017; Takei, 2002), thereby offsetting the signature of the liquid melt.

However, this signal is convolved with a significant change in resolution. Our synthetic tests (Figure S7 in Supporting Information S1) demonstrate that a nearly identical reduction in the anomaly's amplitude is recovered when the later time intervals lack shallow seismicity, even with a static synthetic model. This confirms that the cessation of shallow earthquakes after 24 September (Figure 2) causes a substantial loss of resolution in the uppermost layers. Therefore, while fluid vapourization remains a geologically plausible process during the eruption, its expression in our tomographic models is likely masked and dominated by the resolution artifact. We cannot isolate and quantify the potential physical contribution from the tomographic data alone.

The interaction between the ascending magma and relatively cold, shallow meteoric fluids likely led to the rapid freezing and sealing of some magma pathways. This process of repeated dike arrest and the subsequent formation of new dikes and sills to bypass blocked zones provides a mechanistic explanation for the observed down-slope migration of the eruptive vent over the first few days of the eruption. Essentially, as earlier pathways to the surface were sealed off by quenching, the magma was forced to exploit new, laterally offset fractures, manifesting as a migrating surface vent. Additionally, the massive flashing of meteoric water to steam upon contact with the magma could account for the anomalously strong degassing observed throughout the eruption (e.g., Amonte et al., 2022; Torres-González et al., 2022). Below 8 km depth b.s.l., a prominent high Vp/Vs anomaly is observed in both time intervals, showing minimal change before and after the eruption began (Figure 5). This anomaly was also clearly identified in the previous model by D'Auria et al. (2022), which was based on the entire data set. We propose that this anomaly represents a large magma storage zone accumulated at the base of the crust over an extended preparation period.

As seen in vertical cross-sections in Figure 5, between the deep and shallow high Vp/Vs anomalies, a layer of low Vp/Vs ratio is identified, which was particularly prominent before the eruption onset at depths between 5 and 8 km b.s.l. This layer may represent a rigid barrier at the base of the crust that confined magma within the deeper storage zone over an extended period. As demonstrated by D'Auria et al. (2022), several attempts by magma to breach this barrier were recorded prior to the eruption, evidenced by distinct seismic swarms below 10 km b.s.l. starting as early as 2018.

When comparing the results before and after the eruption onset in the vertical sections in Figure 5, we observe a clear disruption of the rigid barrier by a vertical high Vp/Vs anomaly in the later episode. The core of this anomaly, delineated in the vertical section by the Vp/Vs = 2.05 contour, is interpreted as the primary magma conduit. The broader zone of elevated Vp/Vs ratio (∼1.90–2.05) surrounding this core likely represents a combination of a thermal and fluid-saturated halo around the melt pathway and some vertical smearing due to the limited resolution of the tomography. This conduit-related anomaly aligns spatially and temporally with the well-documented upward migration of seismicity that culminated in the surface eruption (D'Auria et al., 2022). The co-location of this high-Vp/Vs feature with the pathway of ascending seismicity strongly supports its interpretation as the primary magma conduit that fed the 2021 eruption.

In our images, the conduit appears to be approximately 1 km wide, which seems excessively large for a single dike. This could indicate that magma ascent occurred through a system of dispersed fractures occupying a significant volume. Alternatively, the actual size of the conduit zone might be much smaller than what is observed in our images, with the apparent thickness resulting from limited resolution and smearing in our tomography model. In this case, the true properties of the conduit rocks could be significantly more contrasted than those resolved in our model.

The newly formed conduit is located directly beneath the Cumbre Vieja Ridge but is offset approximately 5 km to the southeast of the Tajogaite eruption vent. We interpret this path to be controlled by a pre-existing, weakened zone beneath the volcanic ridge, which has served as a primary magma pathway in previous eruptions. However, the presence of a thick, rigid cap of solidified rock at shallow depths appears to have prevented direct vertical ascent to the ridge crest, instead diverting the magma laterally and resulting in flank eruptions. This interpretation is supported by our tomographic images (Figure 5, vertical section), which show two branching anomalies of high Vp/Vs ratio above the head of the conduit. One branch is sub-vertical and may represent a sealed fissure that failed to reach the surface, while the other, directed toward the northwest, likely delineates the main fissure that served as the effective magma pathway to the Tajogaite eruption vent.

It is interesting to estimate the evolution of the magma conduit after the eruption began, based on the results with varied starting times of the second data set presented in Figure 6. Although these images correspond to overlapping time windows and do not directly depict the time evolution of the seismic structures, they can be used for a qualitative evaluation of magma migration during the eruption. For the models corresponding to the starting time of the second data set between 20 and 28 September 2021, the conduit-related anomaly exhibits a diapir-like shape with a gradually increasing head. In all these cases, the top limit of the plume remains at a consistent depth of 6–7 km b.s.l. In the later stages, with starting times ranging from 30 September to 20 October 2021, the head of the plume appears to detach from the deeper source and begins to ascend. In the latest stage, the upper limit of this anomaly reaches a depth of 3 km b.s.l. Based on these observations, we propose that after the creation of an open conduit on 19 September 2021, a large volume of magma ascended from the deep source through the rigid barrier, creating a system of dispersed fractures over a significantly large area. The total volume of ascended magma appears to have been larger than the volume actually erupted through the vents to the surface. A portion of the magma was likely stored in the upper crust above the barrier, possibly due to insufficient buoyancy or the freezing of conduits following interaction with meteoric fluids.

It would be interesting to investigate the evolution of the magma system beneath Cumbre Vieja after the end of the eruption. However, seismic activity dramatically decreased, resulting in too few paired events in the syn- and post-eruption periods to allow for sufficiently high-resolution repeated tomography.

6. Conclusions

In this study, we focus on uncovering seismic velocity variations beneath La Palma, where significant changes in subsurface structures were expected due to the voluminous effusive eruption that occurred during September–

November 2021. Using body waves from local earthquakes to detect temporal changes in seismic velocities carries inherent risks, as the resulting tomography images can be strongly influenced by variations in source distributions and ray paths. To address this challenge, we carefully selected data from time windows containing identical numbers of events and phase picks, as well as similar distributions of ray paths. We defined two time intervals: the first represents the preparation stage of the eruption, ending on 19 September 2021, just before the eruption began. The second interval starts on 24 September 2021 and spans approximately three months of the active eruption phase. The ability to resolve temporal changes with the available data was validated through a series of synthetic tests.

The repeated tomography presented in this study provides a fascinating insight into the evolution of the magma conduit system during the 2021 Cumbre Vieja eruption. The analysis of seismic structures and their changes over time suggests a complex dynamic process of magma migration, storage, and ascent. The resulting pair of 3D velocity models, particularly the distributions of the Vp/Vs ratio, clearly reveal the key elements of the magma plumbing system and its evolution during the eruption. The high Vp/Vs ratios observed at shallow depths, which show minimal changes after the eruption onset, likely indicate the presence of meteoric fluids saturating the rocks down to approximately 3 km below the surface. Another high Vp/Vs anomaly, located below 8 km depth, remained nearly unchanged throughout the study period, suggesting a stable deep magma reservoir.

In the syn-eruptive stage, we observe a conduit-related anomaly of high Vp/Vs ratio that exhibits a diapir-like shape with a gradually increasing head. Before the eruption onset on 19 September 2021, this anomaly did not exist. By varying the starting time of the second data set, we assessed the evolution of structures during the syn-eruption period. The conduit evolved from a diapir-like structure with a stable head at 6–7 km depth in the early stages of the eruption to an ascending plume reaching 3 km depth in later stages. We propose that the interaction between ascending magma and meteoric fluids led to the freezing of some pathways and the formation of dispersed fractures, contributing to the observed vent migration and strong degassing. Despite the large volume of magma that ascended, only a portion erupted, with the remainder likely stored in the upper crust.

This study highlights the utility of repeated seismic tomography in unraveling the dynamic processes driving effusive eruptions and provides new insights into the evolution of magma systems during volcanic unrest.

Conflict of Interest

The authors declare no conflicts of interest relevant to this study.

Data Availability Statement

All the figures, data and program codes used to produce the results in the paper are available in open access on Zenodo at Koulakov (2025).

Acknowledgments

This research is supported by the Spanish Project "Generacion del Conicimiento 2022," reference PID2022-143083NB-I00, LEARNING, funded by MICIU/AEI/ 10.13039/501100011033 and by FEDER, UE. IK was supported by the Ministry of Education and Science of Russia within the research project FWZZ-2022-0017. The open access of this article is supported by University of Granada/CBUA.

References

Amonte, C., Melián, G. V., Asensio-Ramos, M., Pérez, N. M., Padrón, E., Hernández, P. A., & D'Auria, L. (2022). Hydrogeochemical temporal variations related to the recent volcanic eruption at the Cumbre Vieja Volcano, La Palma, Canary Islands. *Frontiers in Earth Science*, *10*, 1003890. https://doi.org/10.3389/feart.2022.1003890

Anguita, F., & Hernán, F. (2000). The Canary Islands origin: A unifying model. *Journal of Volcanology and Geothermal Research*, *103*(1–4), 1–26. https://doi.org/10.1016/s0377-0273(00)00195-5

Berezhnev, Y., Belovezhets, N., Shapiro, N., & Koulakov, I. (2023). Temporal changes of seismic velocities below Bezymianny volcano prior to its explosive eruption on 20.12. 2017. *Journal of Volcanology and Geothermal Research*, *433*, 107735. https://doi.org/10.1016/j.jvolgeores.2022.107735

Bushenkova, N., Koulakov, I., Senyukov, S., Gordeev, E. I., Huang, H.-H., El Khrepy, S., & Al Arifi, N. (2019). Tomographic images of magma chambers beneath the Avacha and Koryaksky volcanoes in Kamchatka. *Journal of Geophysical Research: Solid Earth*, *124*(9), 9694–9713. https://doi.org/10.1029/2019JB017952

Cabrera-Pérez, I., D'Auria, L., Soubestre, J., Del Pezzo, E., Prudencio, J., Ibáñez, J. M., et al. (2024). 3-D intrinsic attenuation tomography using ambient seismic noise applied to La Palma Island (Canary Islands). *Scientific Reports*, *14*(1), 27354. https://doi.org/10.1038/s41598-024-79076-w

Cabrera-Pérez, I., D'Auria, L., Soubestre, J., Przeor, M., Barrancos, J., García-Hernández, R., et al. (2023). Spatio-temporal velocity variations observed during the pre-eruptive episode of La Palma 2021 eruption inferred from ambient noise interferometry. *Scientific Reports*, *13*(1), 12039. https://doi.org/10.1038/s41598-023-39237-9

Cannata, A., Di Grazia, G., Giuffrida, M., Gresta, S., Palano, M., Sciotto, M., et al. (2018). Space-time evolution of magma storage and transfer at Mt. Etna Volcano (Italy): The 2015–2016 reawakening of Voragine Crater. *Geochemistry, Geophysics, Geosystems*, *19*(2), 471–495. https://doi.org/10.1002/2017gc007296

Carracedo, J. C., Badiola, E. R., Guillou, H., de la Nuez, J., & Pérez Torrado, F. J. (2001). Geology and volcanology of La Palma and El Hierro, Western Canaries. *Estudios Geológicos*, *57*(5–6), 175–273. https://doi.org/10.3989/egeol.01575-6134

Carracedo, J. C., Day, S., Guillou, H., Torrado, F. J. P., Canas, J. A., & Pérez Torrado, F. J. (1998). Hotspot volcanism close to a passive continental margin: The Canary Islands. *Geological Magazine*, *135*(5), 591–604. https://doi.org/10.1017/s0016756898001447

Carracedo, J. C., & Troll, V. R. (2016). *The geology of the Canary Islands*. Elsevier.

Carracedo, J. C., Troll, V. R., Day, J. M., Geiger, H., Aulinas, M., Soler, V., et al. (2022). The 2021 eruption of the Cumbre Vieja volcanic ridge on La Palma, Canary Islands. *Geology Today*, *38*(3), 94–107. https://doi.org/10.1111/gto.12388

D'Auria, L., Koulakov, I., Prudencio, J., Cabrera-Pérez, I., Ibáñez, J. M., Barrancos, J., et al. (2022). Rapid magma ascent beneath La Palma revealed by seismic tomography. *Scientific Reports*, *12*(1), 17654. https://doi.org/10.1038/s41598-022-21818-9

Donaldson, C., Caudron, C., Green, R. G., Thelen, W. A., & White, R. S. (2017). Relative seismic velocity variations correlate with deformation at Kīlauea volcano. *Science Advances*, *3*(6), e1700219. https://doi.org/10.1126/sciadv.1700219

Duputel, Z., Ferrazzini, V., Brenguier, F., Shapiro, N., Campillo, M., & Nercessian, A. (2009). Real time monitoring of relative velocity changes using ambient seismic noise at the Piton de la Fournaise volcano (La Réunion) from January 2006 to June 2007. *Journal of Volcanology and Geothermal Research*, *184*(1–2), 164–173. https://doi.org/10.1016/j.jvolgeores.2008.11.024

Geldmacher, J., Hoernle, K., Bogaard, P. V. D., Duggen, S., & Werner, R. (2005). New 40Ar/39Ar age and geochemical data from seamounts in the Canary and Madeira volcanic provinces: Support for the mantle plume hypothesis. *Earth and Planetary Science Letters*, *237*(1–2), 85–101. https://doi.org/10.1016/j.epsl.2005.04.037

González-de-Vallejo, L., Álvarez-Hernández, A., Ferrer, M., Lockwood, J. P., Pérez, N. M., Hernández, P. A., et al. (2024). La Palma 2021 Eruption (Canary Islands): Measurements and Modelling of Lava Flow Cooling Rates and Applications for Infrastructure Reconstruction and Risk Mitigation. *GeoHazards*, *5*(4), 1093–1124. https://doi.org/10.3390/geohazards5040052

Guillou, H., Carracedo, J. C., & Duncan, R. A. (2001). K–Ar, 40Ar–39Ar ages and magnetostratigraphy of Brunhes and Matuyama lava sequences from La Palma Island. *Journal of Volcanology and Geothermal Research*, *106*(3–4), 175–194. https://doi.org/10.1016/s0377-0273(00)00294-8

Hernández-Pacheco, A., & Valls, M. C. (1982). The historic eruptions of La Palma (Canary Islands). *Journal of Volcanology and Geothermal Research*, *13*(3–4), 261–270.

Husen, S., Smith, R. B., & Waite, G. P. (2004). Evidence for gas and magmatic sources beneath the yellowstone volcanic field from seismic tomographic imaging. *Journal of Volcanology and Geothermal Research*, *131*(3–4), 397–410. https://doi.org/10.1016/s0377-0273(03)00416-5

Kasatkina, E., Koulakov, I., Grapenthin, R., Izbekov, P., Larsen, J., Al Alifi, N., & Qaysi, S. I. (2022). Multiple shallow magma sources beneath the Okmok caldera as inferred from local earthquake tomography. *Journal of Geophysical Research: Solid Earth*, *127*(10), e2022JB024656. https://doi.org/10.1029/2022JB024656

Kasatkina, E., Koulakov, I., West, M., & Izbekov, P. (2014). Seismic structure changes beneath Redoubt Volcano during the 2009 eruption inferred from local earthquake tomography. *Journal of Geophysical Research: Solid Earth*, *119*(6), 4938–4954. https://doi.org/10.1002/2013jb010935

Koulakov, I. (2009). LOTOS code for local earthquake tomographic inversion. Benchmarks for testing tomographic algorithms. *Bulletin of the Seismological Society of America*, *99*(1), 194–214. https://doi.org/10.1785/0120080013

Koulakov, I. (2025). Data and program codes to reproduce the results of repeated seismic tomography to reveal velocity changes during the eruption on La Palma in 2021 [Dataset]. *Zenodo*. https://doi.org/10.5281/zenodo.15036210

Koulakov, I., Gladkov, V., El Khrepy, S., Al-Arifi, N., & Fathi, I. H. (2016). Application of repeated passive source travel time tomography to reveal weak velocity changes related to the 2011 Tohoku-Oki Mw 9.0 earthquake. *Journal of Geophysical Research: Solid Earth*, *121*(6), 4408–4426. https://doi.org/10.1002/2016jb013002

Koulakov, I., Gordeev, E. I., Dobretsov, N. L., Vernikovsky, V. A., Senyukov, S., Jakovlev, A., & Jaxybulatov, K. (2013). Rapid changes in magma storage beneath the Klyuchevskoy group of volcanoes inferred from time-dependent seismic tomography. *Journal of Volcanology and Geothermal Research*, *263*, 75–91. https://doi.org/10.1016/j.jvolgeores.2012.10.014

Koulakov, I., Plechov, P. Y., Mania, R., Walter, T. R., Smirnov, S. Z., Abkadyrov, I., et al. (2021). Anatomy of the Bezymianny volcano merely before an explosive eruption on 20.12.2017. *Scientific Reports*, *11*(1), 1758. https://doi.org/10.1038/s41598-021-81498-9

Koulakov, I., Smirnov, S. Z., Gladkov, V., Kasatkina, E., West, M., El Khrepy, S., & Al-Arifi, N. (2018). Causes of volcanic unrest at Mt. Spurr in 2004–2005 inferred from repeated tomography. *Scientific Reports*, *8*(1), 17482. https://doi.org/10.1038/s41598-018-35453-w

Koulakov, I., & Vargas, C. A. (2018). Evolution of the magma conduit beneath the Galeras volcano inferred from repeated seismic tomography. *Geophysical Research Letters*, *45*(15), 7514–7522. https://doi.org/10.1029/2018gl078850

Kuster, G. T., & Toksoz, M. N. (1974). Velocity and attenuation of seismic waves in two-phase media: Part II. Experimental results. *Geophysics*, *39*(5), 607–618. https://doi.org/10.1190/1.1440451

Kuznetsov, P. Y., Koulakov, I., Jakovlev, A., Abkadyrov, I., Deev, E., Gordeev, E. I., et al. (2017). Structure of volatile conduits beneath gorely Volcano (Kamchatka) revealed by local earthquake tomography. *Geosciences*, *7*(4), 111. https://doi.org/10.3390/geosciences7040111

Lin, G., Amelung, F., Shearer, P. M., & Okubo, P. G. (2015). Location and size of the shallow magma reservoir beneath Kılauea caldera, constraints from near-source Vp/Vs ratios. *Geophysical Research Letters*, *42*(20), 8349–8357. https://doi.org/10.1002/2015GL065802

Masson, D. G., Watts, A. B., Gee, M. J. R., Urgeles, R., Mitchell, N. C., Le Bas, T. P., & Canals, M. (2002). Slope failures on the flanks of the western Canary Islands. *Earth-Science Reviews*, *57*(1–2), 1–35. https://doi.org/10.1016/s0012-8252(01)00069-1

Nolet, G. (1987). Seismic wave propagation and seismic tomography. In *Seismic tomography: With applications in global seismology and exploration geophysics* (pp. 1–23). Dordrecht: Springer Netherlands.

Olivier, G., Brenguier, F., Carey, R., Okubo, P., & Donaldson, C. (2019). Decrease in seismic velocity observed prior to the 2018 eruption of Kīlauea volcano with ambient seismic noise interferometry. *Geophysical Research Letters*, *46*(7), 3734–3744. https://doi.org/10.1029/2018gl081609

Paige, C. C., & Saunders, M. A. (1982). LSQR: An algorithm for sparse linear equations and sparse least squares. *ACM Transactions on Mathematical Software*, *8*(1), 43–71. https://doi.org/10.1145/355984.355989

Patanè, D., Barberi, G., Cocina, O., De Gori, P., & Chiarabba, C. (2006). Time-resolved seismic tomography detects magma intrusions at Mount Etna. *Science*, *313*(5788), 821–823. https://doi.org/10.1126/science.1127724

Romero, J. E., Burton, M., Cáceres, F., Taddeucci, J., Civico, R., Ricci, T., et al. (2022). The initial phase of the 2021 Cumbre Vieja ridge eruption (Canary Islands): Products and dynamics controlling edifice growth and collapse. *Journal of Volcanology and Geothermal Research*, *431*, 107642. https://doi.org/10.1016/j.jvolgeores.2022.107642

Sens-Schönfelder, C., Pomponi, E., & Peltier, A. (2014). Dynamics of Piton de la Fournaise volcano observed by passive image interferometry with multiple references. *Journal of Volcanology and Geothermal Research*, *276*, 32–45. https://doi.org/10.1016/j.jvolgeores.2014.02.012

Sens-Schönfelder, C., & Wegler, U. (2006). Passive image interferometry and seasonal variations of seismic velocities at Merapi Volcano, Indonesia. *Geophysical Research Letters*, *33*(21), L21302. https://doi.org/10.1029/2006GL027797

Serrano, I., Dengra, M. A., Almendros, F. J., Torcal, F., & Zhao, D. (2023). Seismic anisotropy tomography beneath La Palma in the canary islands, Spain. *Journal of Volcanology and Geothermal Research*, *441*, 107870. https://doi.org/10.1016/j.jvolgeores.2023.107870

Shearer, P. M. (1988). Cracked media, Poisson's ratio and the structure of the upper oceanic crust. *Geophysical Journal International*, *92*(2), 357–362. https://doi.org/10.1111/j.1365-246X.1988.tb01149.x

Sparks, R. S. J., Annen, C., Blundy, J. D., Cashman, K. V., Rust, A. C., & Jackson, M. D. (2019). Formation and dynamics of magma reservoirs. *Philosophical Transactions of the Royal society A*, *377*(2139), 20180019. https://doi.org/10.1098/rsta.2018.0019

Takei, Y. (2002). Effect of pore geometry on vP/vS: From equilibrium geometry to crack. *Journal of Geophysical Research*, *107*(B2), 2043. https://doi.org/10.1029/2001JB000522

Torres-González, P. A., Luengo-Oroz, N., Lamolda, H., & D'Alessandro, W. (2022). Monitoring the 2021 Cumbre Vieja eruption (La Palma, Canary Islands): Insights from seismic and geochemical data. *Scientific Reports*, *12*(1), 1–12.

Vargas, C. A., Koulakov, I., Jaupart, C., Gladkov, V., Gomez, E., El Khrepy, S., & Al-Arifi, N. (2017). Breathing of the Nevado del Ruiz volcano reservoir, Colombia, inferred from repeated seismic tomography. *Scientific Reports*, *7*(1), 46094. https://doi.org/10.1038/srep46094

Yaroshenko, G., Koulakov, I., Al-Arifi, N., Qaysi, S., & El-Khrepy, S. (2022). Structure of the magma plumbing system beneath Semisopochnoi Island (Aleutian Arc) inferred from seismic tomography. *Scientific Reports*, *12*(1), 10771. https://doi.org/10.1038/s41598-022-14794-7

Erratum

The originally published version of this article contained errors in the Acknowledgments and author affiliations. The following has been added to the end of the Acknowledgments: "The open access of this article is supported by University of Granada/CBUA." The following affiliation has been added for coauthor Jesús M. Ibáñez: Andalusian Institute of Geophysics, Universidad de Granada, Granada, Spain. This may be considered the authoritative version of record.